CSMA 2026
17ème Colloque National en Calcul des Structures
18-22 Mai 2026, Presqu'île de Giens (Var)

Aeroelastic optimization of a long aspect ratio wing model to trigger coupled-mode flutter

S. Dosse[1], X. Amandolese[1], J.-F. Deü[1], C. Hoareau[1]

[1] *LMSSC, Conservatoire National des Arts et Métiers, 292 Rue Saint-Martin, Paris 75003, France, simon.dosse@lecnam.net*

Abstract — This study aims to design a long aspect ratio wing model to be tested in a wind tunnel, focusing on the aeroelastic phenomenon of coupled-mode flutter. Starting from a previously tested taut-strip model, the objective is to identify a set of aeroelastic parameters that minimize the flutter speed. To do so, an experimentally validated aeroelastic model is used along with an optimization approach. A configuration exhibiting an unstable B1/T1 aeroelastic mode that optimizes the fluid-structure energy transfer is identified and discussed.

Keywords — aeroelasticity, coupled-mode flutter, elastic wing, fluid-structure interaction, reduced-order modeling

1 Introduction

In recent years, the study of aeroelastic phenomena in long aspect ratio wings has gained significant attention due to its implications in both aerospace and energy fields. In this context, this work focuses on high aspect-ratio lifting surfaces operating in subsonic regimes, which are commonly encountered in applications such as solar-powered UAV wings, High Altitude Long Endurance (HALE) drones and large wind turbine blades. These structures often undergo static and dynamic deformations, raising concerns about whether traditional aeroelastic models can accurately predict flutter onset and post-critical behavior.

Among aeroelastic instabilities, the coupled-mode flutter has been the most studied aeroelastic instability due to its critical implications for structures safety. Its mechanisms have been widely detailed in fundamental aeroelasticity texts. The instability arises from the coupling of structural modes, typically bending and torsion. As the flow velocity approaches a critical threshold, the associated modal frequencies tend to converge. This near-coalescence is associated with the emergence of an unstable aeroelastic mode allowing the transfer of energy from the flow to the structure. This results in large-amplitude self-sustained oscillations.

Several experimental and numerical studies have been conducted to investigate coupled-mode flutter. Among studies dedicated to elastic wings, few have been supported by experimental models. We can cite the one made by Tang and Dowell [1], the Pazywing [2], the flexible wing designed by Stephan and Amandolese [3] and the one built at the University of Bristol [4]. A 1.5 meter elastic wing model was also recently tested in one of the Iat-Cnam wind tunnel. Equipped with piezoelectric patches in order to validate control strategies, this wing model was supposed to flutter in the velocity range of the wind tunnel but did not do so due to a particular aeroelastic mode behavior involving a second bending and first torsional mode [5].

In that context, the objective of this study is to adapt the design of this wing model to achieve the lowest possible critical flutter speed by optimizing some of the wing aeroelastic parameters. To do so, a previously validated aeroelastic model [5] that captures the essential dynamics is used, along with an optimization based on a genetic algorithm. In a long term perspective, this wing model will serve as an experimental benchmark to validate more advanced nonlinear aeroelastic models that account for large deformations and post-critical fluid-structure interactions. Moreover, it will be used to test flutter control strategies.

The paper is organized as follows. First, the aeroelastic model used to represent the wing's dynamics is presented, including the linear structural and unsteady aerodynamic components. Next, the optimization approach employed to minimize the flutter speed is described and the results are discussed.

2 Aeroelastic model

The experimental wing model is designed following a taut-strip architecture in order to separate the structural and aerodynamic parameters as clearly as possible [3]. It is based on an internal beam that ensures the stiffness in normal bending and torsion, to which NACA0015 rigid strip sections are fixed to form the aerodynamic surface of the wing as seen in Figure 2.1a. A schematic of the wing model is shown in Figure 2.1b.

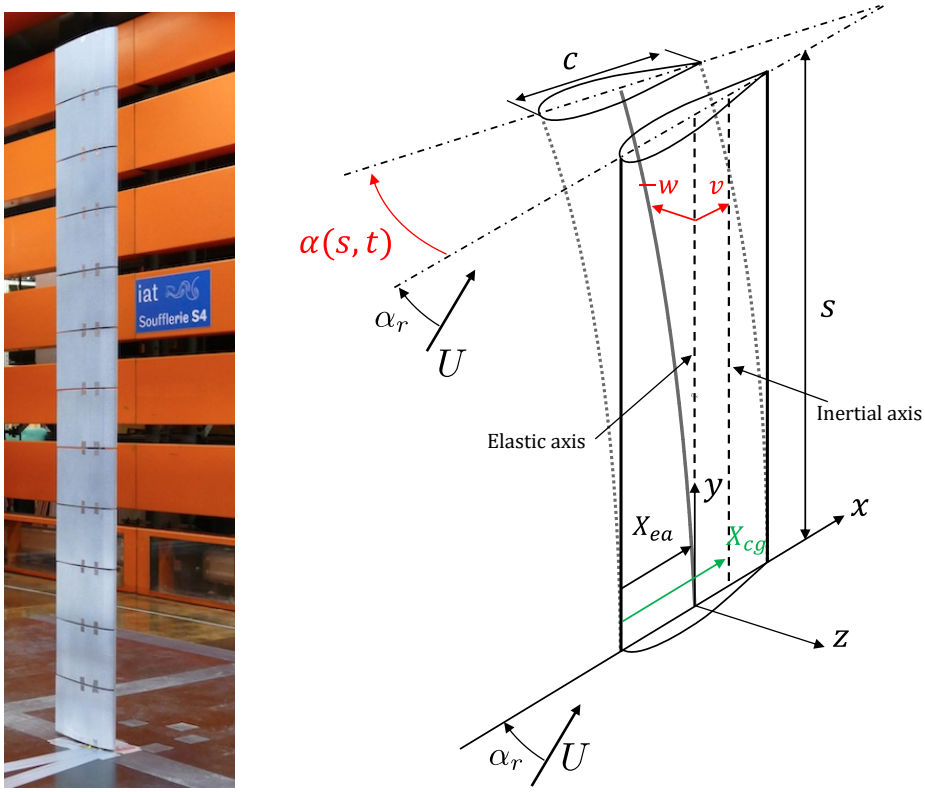

(a) (b)

Figure 2.1: (a) View of the taut-strip wing model in wind tunnel. (b) Schematic of the wing model. The dotted grey lines illustrate the deformed configuration. Red annotations indicate the degrees of freedom.

The wing is modeled as a cantilever beam with bending and torsional degrees of freedom, following the linear Hodges-Dowell beam theory described in [6]. The chordwise displacement is neglected as it does not introduce any coupling term in the linear domain. The angle of attack α_r will also be assumed to be zero. The dynamics are governed by the following linear equations of motion

$$\begin{aligned} m\ddot{w} + c_w\dot{w} + (EI_x w'')'' + mX_\alpha\ddot{\alpha} &= -F_N, \\ I_\alpha\ddot{\alpha} + c_\alpha\dot{\alpha} - (GJ\alpha')' + mX_\alpha\ddot{w} &= M, \end{aligned} \tag{2.1}$$

where $w(y,t)$ is the bending displacement of the elastic axis, which is positively defined along the z-axis, $\alpha(y,t)$ is the torsional rotation about the elastic axis, which is considered positive when evolving clockwise around the y-axis, m and I_α are the mass and mass moment of inertia about the elastic axis per unit length, c_w and c_α are the viscous damping coefficients, EI_x and GJ are the stiffness in bending and torsion. $F_N(y,t)$ is the distributed normal force, which is aligned with the negative z-axis, $M(y,t)$ is the distributed moment of the aerodynamic forces about the elastic axis. These loads are defined by the aerodynamic model. As α stays small, F_N can be approximated as $F_N \approx L$, where L is the lift force orthogonal to the incoming flow direction. In the following, L will be used. The coupling terms $mX_\alpha\ddot{\alpha}$ and $mX_\alpha\ddot{w}$ arise due to the offset between the elastic and inertial axes, where X_α is the distance between these two axes such as $X_\alpha = X_{\text{cg}} - X_{\text{ea}}$. The used models are summarized in Figure 2.2.

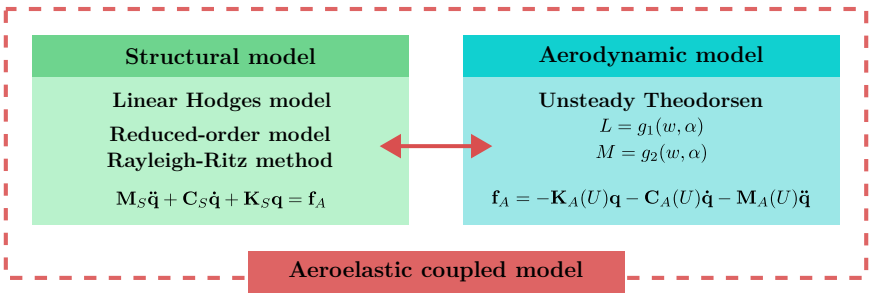

Figure 2.2: Summary of models used in this study.

2.1 Structural model

The Rayleigh-Ritz method is employed to represent the system's deformations by a finite series of assumed mode shapes, each multiplied by an unknown time-dependent generalized coordinate. The displacement $w(y,t)$ and rotation $\alpha(y,t)$ are approximated as follows:

$$w(y,t) = \sum_{i=1}^{N_w} \phi_{w,i}(y) q_{w,i}(t), \quad \alpha(y,t) = \sum_{i=1}^{N_\alpha} \phi_{\alpha,i}(y) q_{\alpha,i}(t) \tag{2.2}$$

where $\phi_{w,i}(y)$ and $\phi_{\alpha,j}(y)$ are the assumed mode shapes for bending and torsion respectively, while $q_{w,i}(t)$ and $q_{\alpha,i}(t)$ are the corresponding generalized coordinates. N_w and N_α denote the number of bending and torsional modes considered in the approximation. The bending and torsion modes $\phi_{w,i}$ and $\phi_{\alpha,i}$ are provided in [5]. Using Equation (2.2) in Equation (2.1), the structural model can be expressed in matrix form as

$$\mathbf{M}_S\ddot{\mathbf{q}} + \mathbf{C}_S\dot{\mathbf{q}} + \mathbf{K}_S\mathbf{q} = \mathbf{f}_A, \tag{2.3}$$

with $\mathbf{q} = [q_{w,1}(t), \ldots, q_{w,N_w}, q_{\alpha,1}(t), \ldots, q_{\alpha,N_\alpha}(t)]^T$ the vector of generalized coordinates. $\mathbf{M_S}$, $\mathbf{C}_S$ and $\mathbf{K}_S$ are respectively the mass, damping and stiffness structural matrices, and $\mathbf{f}_A$ is the vector of generalized aerodynamic forces that includes L and M. The expressions of these matrices and the aerodynamic forces are detailed in [5]. Note that as the elastic and inertial axis do not coincide, the mass matrix $\mathbf{M}_S$ is not diagonal. Indeed, inertial coupling terms $mX_\alpha\ddot{\alpha}$ and $mX_\alpha\ddot{w}$ appear in Equation (2.1). Then, a structural coupling exists between bending and torsion even in the absence of aerodynamic forces.

2.2 Aerodynamic model

The aerodynamic model defines the aerodynamic loads L and M contained in $\mathbf{f}_A$ acting on the wing due to its motion in the airflow. They are function of the lift and moment coefficients C_L and C_M. The latter strongly depend on the reduced frequency which is a key nondimensional parameter defined as $k = \frac{\omega b}{U}$ where ω is the oscillation frequency of the considered mode, b is the semi-chord of the wing and U is the free-stream velocity. Low values of k correspond to a regime where the quasi-steady assumptions are valid, whereas higher k values indicate significant unsteady aerodynamic effects. In this study, the Theodorsen's unsteady aerodynamic based on potential and incompressible flow theory will be used. It introduces the concept of a continuous vortex shed from the trailing edge. The resulting vortex system, formed by spanwise-aligned vortices convected downstream, induces a velocity field that alters the local flow around the airfoil. Using the Theodorsen's formulation with the Wright and Cooper's notation, it leads to

$$\begin{aligned} L(y,t) &= \rho U^2 \left(L_w w + L_{\dot{w}} \frac{b\dot{w}}{U} + L_{\ddot{w}} \frac{b^2\ddot{w}}{U^2} + L_\alpha b\alpha + L_{\dot{\alpha}} \frac{b^2\dot{\alpha}}{U} + L_{\ddot{\alpha}} \frac{b^3\ddot{\alpha}}{U^2} \right), \\ M(y,t) &= \rho U^2 b \left(M_w w + M_{\dot{w}} \frac{b\dot{w}}{U} + M_{\ddot{w}} \frac{b^2\ddot{w}}{U^2} + M_\alpha b\alpha + M_{\dot{\alpha}} \frac{b^2\dot{\alpha}}{U} + M_{\ddot{\alpha}} \frac{b^3\ddot{\alpha}}{U^2} \right), \end{aligned} \tag{2.4}$$

where L_w, $L_{\dot{w}}$, $L_{\ddot{w}}$, L_α, $L_{\dot{\alpha}}$, $L_{\ddot{\alpha}}$, M_w, $M_{\dot{w}}$, $M_{\ddot{w}}$, M_α, $M_{\dot{\alpha}}$ and $M_{\ddot{\alpha}}$ are defined in [7].

Recalling that w and α are approximated using the Rayleigh-Ritz method in terms of generalized coordinates q_w and q_α, see Equation (2.2), the generalized aerodynamic forces $\mathbf{f}_A$ can then be written as

$$\mathbf{f}_A = -\mathbf{K}_A(U)\mathbf{q} - \mathbf{C}_A(U)\dot{\mathbf{q}} - \mathbf{M}_A(U)\ddot{\mathbf{q}} \tag{2.5}$$

where we identify the aerodynamic stiffness matrix $\mathbf{K}_A(U)$, damping matrix $\mathbf{C}_A(U)$ and mass matrix $\mathbf{M}_A(U)$ which depend on the free-stream velocity U.

2.3 Fluid-structure interaction model

Combining the structural model Equation (2.3) and the aerodynamic forces Equation (2.5), the fluid-structure interaction model can be written as follows

$$\mathbf{M}(U)\ddot{\mathbf{q}} + \mathbf{C}(U)\dot{\mathbf{q}} + \mathbf{K}(U)\mathbf{q} = 0, \tag{2.6}$$

such that $\mathbf{M}(U) = \mathbf{M}_S + \mathbf{M}_A(U)$, $\mathbf{C}(U) = \mathbf{C}_S + \mathbf{C}_A(U)$ and $\mathbf{K}(U) = \mathbf{K}_S + \mathbf{K}_A(U)$.

In a state-space approach, with a state vector $\mathbf{x} = [\mathbf{q}\ \dot{\mathbf{q}}]^T$, the system Equation (2.6) becomes

$$\dot{\mathbf{x}} = \mathbf{A}(U)\mathbf{x} \quad \text{with} \quad A(U) = \begin{bmatrix} \mathbf{0} & \mathbf{I} \\ -\mathbf{M}(U)^{-1}\mathbf{K}(U) & -\mathbf{M}(U)^{-1}\mathbf{C}(U) \end{bmatrix}. \tag{2.7}$$

This state-space will be used numerically to compute the eigenvalues of the matrix $\mathbf{A}(U)$ and determine the stability of the aeroelastic coupled system at a given velocity U. The aeroelastic modes are denoted by $\mathbf{v}^i$ where the superscript i refers to the mode number, such as:

$$\mathbf{v}^i = \begin{pmatrix} \mathbf{v}^i_w \\ \mathbf{v}^i_\alpha \end{pmatrix} \quad \text{with} \quad \mathbf{v}^i_w = \begin{pmatrix} v^i_{w,1} \\ \dots \\ v^i_{w,N_w} \end{pmatrix}, \quad \mathbf{v}^i_\alpha = \begin{pmatrix} v^i_{\alpha,1} \\ \dots \\ v^i_{\alpha,N_\alpha} \end{pmatrix}. \tag{2.8}$$

Each aeroelastic mode is characterized by its eigenvalues $\lambda_i = \delta_i + j\omega_i$. The damping ratio ζ_i of each mode can be computed as

$$\zeta_i = -\operatorname{sign}(\delta_i)\left(1 + \left(\frac{\omega_i}{\delta_i}\right)^2\right)^{-1/2}. \tag{2.9}$$

The flutter critical velocity U_c is defined as the velocity for which the damping ratio of an aeroelastic mode becomes zero while increasing U, such as

$$\begin{cases} \zeta_i(U_c) = 0 \\ \dfrac{d\zeta_i}{dU}(U_c) < 0 \end{cases}. \tag{2.10}$$

Figure 2.3 shows the frequencies and damping ratios of the three first aeroelastic modes as a function of the velocity U, computed using the aeroelastic parameters of the reference wing tested at the Iat-Cnam wind tunnel [5]. One can observe that despite the merging of the second aeroelastic branch ($\mathbf{v}^2$) with the third aeroelastic branch ($\mathbf{v}^3$) beyond $U \approx 28m/s$, no flutter can occur in the velocity range of the wind tunnel. Indeed, although slightly decreasing beyond $U \approx 25m/s$, the damping of the potentially unstable aeroelastic mode, i.e. $\mathbf{v}^2$, stays positive, indicating stability.

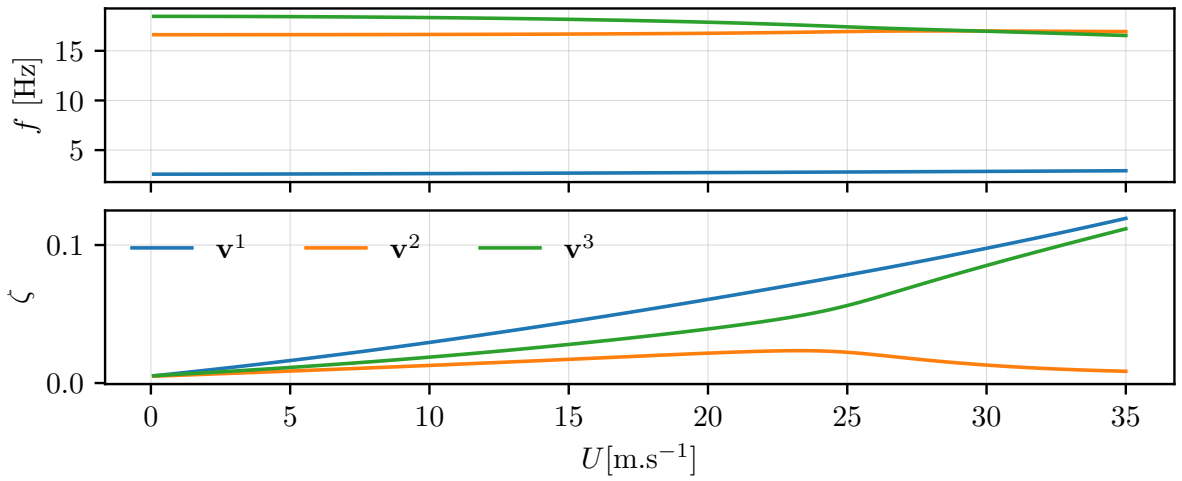

Figure 2.3: Frequencies and damping ratios of the three first aeroelastic modes of the reference wing tested at the Iat-Cnam wind tunnel [5] as a function of the velocity U.

In the next section, the optimization procedure used to minimize the flutter speed U_c is presented. The results are then discussed.

3 Aeroelastic parameters optimization

In this study, the objective is to minimize the critical flutter speed U_c of the wing by optimizing some of its aeroelastic parameters. All the sections along the span are assumed to be identical. The design variables considered for optimization include the elastic axis position X_{ea}, the inertial axis position X_{cg}, the spanwise bending stiffness EI_x, and the torsional stiffness GJ. Note that modifying the position of the elastic and inertial axis makes the moment of inertia per unit length I_α vary as well. The optimization problem can be formulated as follows:

$$\begin{aligned} \min_{X_{\text{ea}}, X_{\text{cg}}, EI_x, GJ} \quad & U_c(X_{\text{ea}}, X_{\text{cg}}, EI_x, GJ) \\ \text{subject to} \quad & X_{\text{ea}}^{\min} \leq X_{\text{ea}} \leq X_{\text{ea}}^{\max},\ X_{\text{cg}}^{\min} \leq X_{\text{cg}} \leq X_{\text{cg}}^{\max}, \\ & EI_x^{\min} \leq EI_x \leq EI_x^{\max},\ GJ^{\min} \leq GJ \leq GJ^{\max}. \end{aligned} \tag{3.1}$$

The boundaries of the design variables are based on realistic considerations and manufacturing constraints. Without any explicit expression for U_c as a function of the design variables, a gradient-free optimization algorithm is employed. As several parameters interact with each other, the cost function must be non-convex and may present multiple local minima. Therefore, a genetic algorithm optimization method is preferred. In this study, the *Differential Evolution* (DE) [8] algorithm is used to solve the optimization problem Equation (3.1). DE is a population-based stochastic optimization technique that iteratively improves a population of candidate solutions based on mutation, crossover, and selection operations. The algorithm starts with an initial population of potential solutions, which are randomly generated within the defined bounds of the design variables. At each iteration, new candidate solutions are created by combining existing ones through mutation and crossover operations. The best-performing candidates are selected to form the next generation, and the process continues until convergence criteria are met.

For some sets of parameters, the wing may not exhibit any instability. Hence, the cost function has some indeterminate regions. In such cases, the optimization algorithm is designed to discard these configurations by assigning them a high penalty value for U_c, effectively removing them from consideration in the optimization process. The other parameters not considered in the optimization problem are set constant and reported in Table 3.1.

Name	Symbol	Value	Unit
Semi span	s	2	m
Chord	c	0.20	m
Mass per unit length	m	2.4	$\mathrm{kg.m^{-1}}$

Table 3.1: Considered parameters for the wing model.

3.1 Results and discussion

The parameters obtained from the optimization process are reported in Table 3.2. The associated section is drawn in Figure 3.1.

Name	Symbol	Value	Unit
Distance of the elastic axis from the leading edge	X^*_{ea}	0.087	m
Distance of the inertial axis from the leading edge	X^*_{cg}	0.12	m
Moment of inertia (about the elastic axis) per unit length	I^*_α	0.011	$\mathrm{kg.m^2.m^{-1}}$
Spanwise bending stiffness	EI^*_x	475	$\mathrm{N.m^2}$
Torsional stiffness	GJ^*	40	$\mathrm{N.m^2}$

Table 3.2: Optimal parameters of the NACA0015 wing section to minimize the flutter speed U_c.

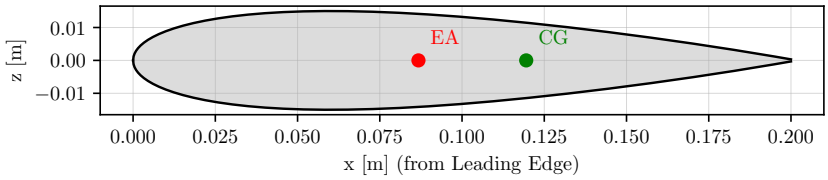

Figure 3.1: Optimal NACA0015 wing section result.

The frequencies and damping ratios of the three first aeroelastic modes of the optimized wing are plotted as a function of the incoming flow velocity U in Figure 3.2. One can observe that a flutter speed is numerically reached at $U_c = 23.2\,\mathrm{m.s^{-1}}$. It concerns the second aeroelastic mode ($\mathbf{v}^2$) that also exhibits a significant negative rate $\frac{d\zeta_2}{dU}(U_c)$, indicating a clear flutter scenario.

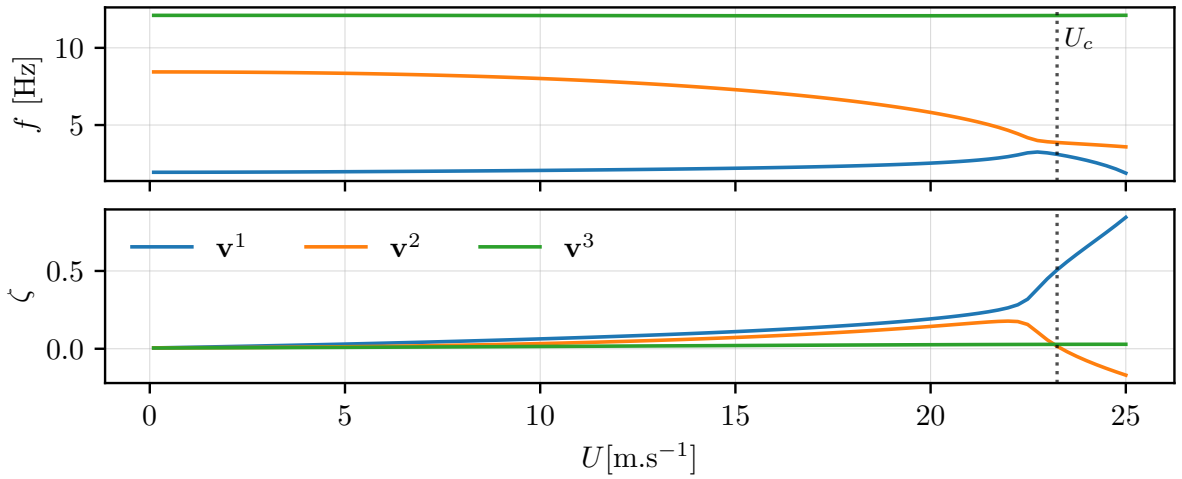

Figure 3.2: Frequencies and damping ratios of the three first aeroelastic modes of the optimal wing as a function of the velocity U.

It also appears that the components of the unstable aeroelastic mode have changed compared with the reference wing. The contributions of the assumed mode shapes in the second aeroelastic mode $\mathbf{v}^2$ are

illustrated in Figure 3.3 at $U = 25\,\mathrm{m.s^{-1}}$ for the optimal wing and $U = 35\,\mathrm{m.s^{-1}}$ for the reference wing. Regarding the reference wing, $\mathbf{v}^2$ is composed of a second bending mode **B2** coupled with a first torsion mode **T1**. For the optimal wing the unstable aeroelastic mode $\mathbf{v}^2$ is the consequence of a coupling of the first bending mode **B1** with the first torsional mode **T1**.

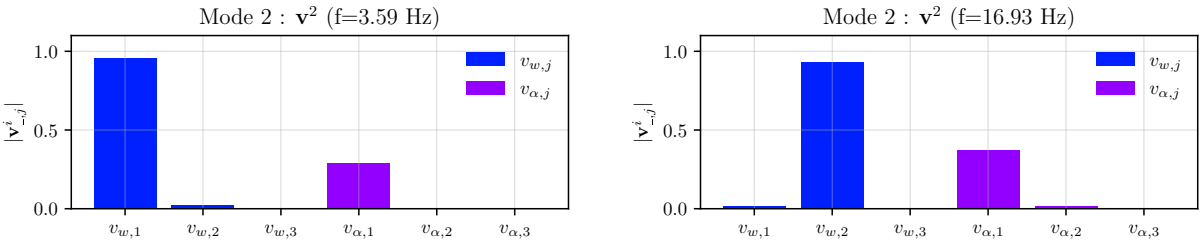

(a) (b)

Figure 3.3: Contributions of the assumed mode shapes in the second aeroelastic mode $\mathbf{v}^2$. (a) For the optimal wing at $U = 25\,\mathrm{m.s^{-1}}$. (b) For the reference wing at $U = 35\,\mathrm{m.s^{-1}}$.

From a given eigenvector $\mathbf{v}^i$, a physical motion shape along the span can be built to compute the work done by the aerodynamic forces over a period $T = \frac{2\pi}{\omega_i}$ as

$$w^i(y,t) = \Re\left\{e^{\omega_i t}\sum_{k=1}^{N_w}\phi_{w,k}(y)v^i_{w,k}\right\}, \quad \alpha^i(y,t) = \Re\left\{e^{\omega_i t}\sum_{k=1}^{N_\alpha}\phi_{\alpha,k}(y)v^i_{\alpha,k}\right\}, \tag{3.2}$$

$$W^i_{\text{aero}}(y) = \int_0^T \left[-L^i(y,t)\dot{w}^i(y,t) + M^i(y,t)\dot{\alpha}^i(y,t)\right] dt. \tag{3.3}$$

The work done by the aerodynamic forces over one period along the span, defined in Equation (3.3), is represented in Figure 3.4 for the unstable $\mathbf{v}^2$ mode (**B1/T1**) of the optimal wing and the potential unstable $\mathbf{v}^2$ mode (**B2/T1**) of the reference wing.

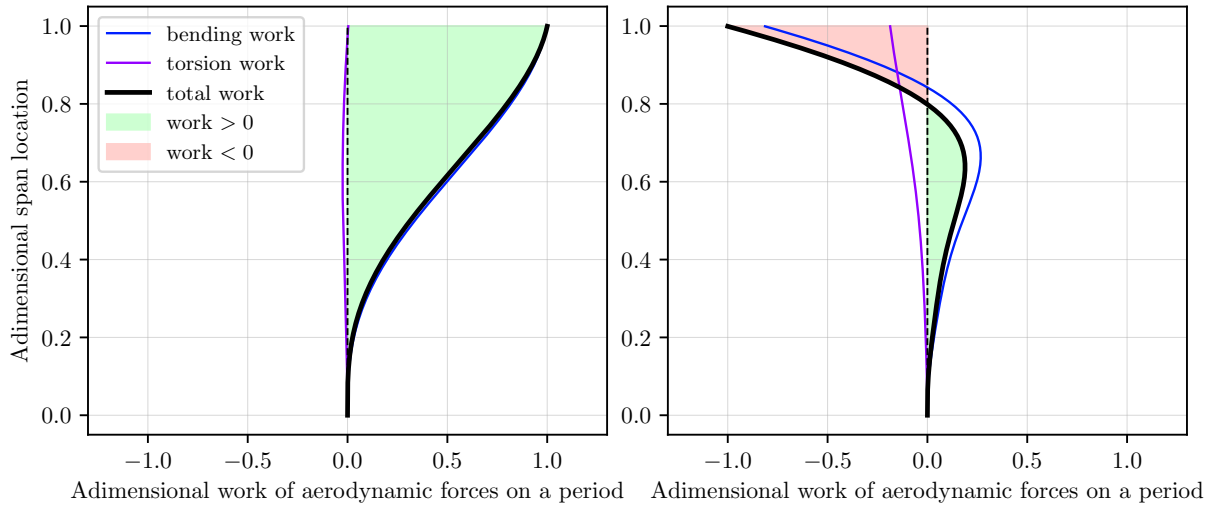

Figure 3.4: Work of the aerodynamic forces over one period along the span for the unstable $\mathbf{v}^2$ mode **B1/T1** of the optimal wing (left) and the potential unstable $\mathbf{v}^2$ mode **B2/T1** of the reference wing (right).

Results show that the **B2/T1** configuration exhibits a positive energy transfer area up to 80% of the span but a larger negative energy transfer area close to the tip of the wing. On the other hand the **B1/T1** unstable mode of the optimized wing is characterized by a positive energy transfer all along the span. The energy transfer is strongly linked to the phase shift between the bending and torsional DOFs. A bending ahead of the torsion leads to a positive work [9]. This condition is reached for the unstable **B1/T1** aeroelastic mode. On the other hand, the B2 shape, which is characterized by a vibration node, does not

have a constant sign along the span. As a consequence the aeroelastic mode plotted in Figure 3.4 (right) exhibits two regions but only one, up to 80% of the span, with an appropriate phase shift.

The energy transfer is illustrated in Figure 3.5, which shows two phase-shift configurations. When the bending is ahead of the torsion, these two DOFs work together to extract energy from the flow.

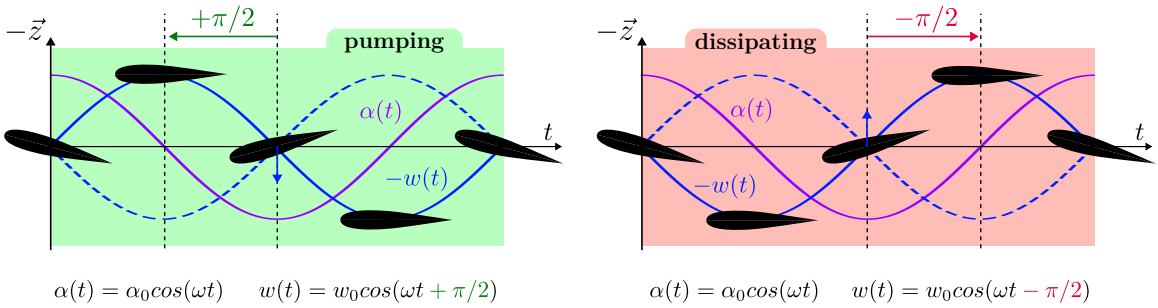

$\alpha(t) = \alpha_0 cos(\omega t)$ $w(t) = w_0 cos(\omega t + \pi/2)$ $\alpha(t) = \alpha_0 cos(\omega t)$ $w(t) = w_0 cos(\omega t - \pi/2)$

Figure 3.5: Energy transfer mechanism between bending and torsion depending on their phase shift.

4 Conclusions

This study presents an optimization approach, employing a genetic algorithm, to minimize the critical flutter speed of a long aspect ratio wing by adjusting its aeroelastic parameters. Adjusting both the elastic and inertial axis positions along with the spanwise bending and torsional stiffness, the optimized wing exhibits numerically a coupled-mode flutter that allows a large energy transfer area along the span, highlighting the importance of mode selection in aeroelastic design. Future work will focus on experimental validation of the optimized wing and further refinement of the aeroelastic model to account for post-critical behavior and geometrical nonlinearity with a FEM approach.

References

[1] Tang, D., Dowell, E. H., "Experimental and Theoretical Study on Aeroelastic Response of High-Aspect-Ratio Wings", *AIAA Journal*, Vol. 39, No. 8, pp. 1430–1441, 2001.

[2] Drachinsky, A., Avin, O., Raveh, D. E., Ben-Shmuel, Y., Tur, M., "Flutter Tests of the Pazy Wing", *AIAA Journal*, Vol. 60, No. 9, pp. 5414–5421, 2022.

[3] Stephan, C., Amandolese, X., "Design and Experimental Tests of a Flexible Wing of High Aspect Ratio for Investigating Flutter Mechanisms", in *Proceedings of IFASD 2024*, La Haye, Netherlands, June 2024.

[4] Jayatilake, S., Lowenberg, M., Woods, B. K. S., Titurus, B., "Nonlinear Aeroelastic Modelling and Analysis of a Geometrically Nonlinear Wing with Combined Unsteady Sectional and Lifting Line Aerodynamics", *Nonlinear Dynamics*, Vol. 113, No. 12, pp. 14657–14693, 2025.

[5] Maxime, P., *Aeroelastic Analysis of a Slender Wing: Wind Tunnel Tests and Modelling*, MatheO ULiège, 2025.

[6] Hodges, D. H., *Nonlinear Composite Beam Theory*, Progress in Astronautics and Aeronautics, Vol. 213, American Institute of Aeronautics and Astronautics, Reston, Va, 2006.

[7] Wright, J. R., Cooper, J. E., *Introduction to Aircraft Aeroelasticity and Loads*, John Wiley & Sons, 2008.

[8] Deb, K., Anand, A., Joshi, D., "A Computationally Efficient Evolutionary Algorithm for Real-Parameter Optimization", *Evolutionary Computation*, Vol. 10, No. 4, pp. 371–395, 2002.

[9] Bisplinghoff, R. L., Ashley, H., *Principles of Aeroelasticity*, Dover Publications, 2013.